Progress In Electromagnetics Research, PIER 84, 407–436, 2008

APPLICATION OF ARTIFICIAL GROUND PLANES IN DUAL-BAND ORTHOGONALLY-POLARIZED LOW-PROFILE HIGH-GAIN PLANAR ANTENNA DESIGN

A. Foroozesh, M. Ng Mou Kehn, and L. Shafai

Department of Electrical and Computer Engineering
University of Manitoba
75A Chancellor's Circle, Winnipeg, MB R3T 5V6, Canada

Abstract—Application of artificial ground planes in design of compact cavity-resonance dual-band high-gain antennas is presented. The artificial ground plane consists of periodic strip grating on grounded dielectric slab. A code based on method of moment (MoM) is developed to analyze and design such artificial ground planes. The reflection parameters obtained using the MoM code are employed to characterize the surface impedance of the artificial ground plane for different incident angles and both TE and TM polarizations. Then, this impedance surface is used in transverse equivalent network (TEN) model of the cavity-resonance antenna with high-permittivity dielectric superstrate. Using TEN model radiation properties of such antennas are analyzed. Finally, the antenna with the compact size is designed to demonstrate the maximum directivity. An interesting characteristic of this antennas is that when the antenna ground plane acts as an artificial magnetic conductor the height of the antenna is almost reduced by a factor of two, while its directivity is increased by about 1 dB compared to the conventional antennas of this class having PEC ground plane.

1. INTRODUCTION

Artificial surfaces find numerous applications in antenna design and microwave engineering [1]. One of these applications is low-profile high-gain cavity-resonance antenna design when such a surface is used as the ground plane [2–4]. Although, the superstrate used in [2] was a highly reflective frequency reflective surface (HR-FSS) consisting of periodic patches, it was shown in [5, 6] that other cavity-resonance antennas with high-permittivity dielectric superstrates can be made low-profile

using artificial ground planes. An artificial ground plane usually consists of a grounded dielectric slab loaded by periodic metallic patches, rings or other frequency selective surface (FSS) shapes. In practical applications, these periodic structures must be truncated. On one hand, using limited number of unit cells degrades the performance of the antenna and prevents achieving the expected high-gain [5, 6]. On the other hand, conventional full-wave analysis (such as MoM, FEM and FDTD) of large periodic structures in presence of the excitation antenna is cumbersome, time-consuming and needs excessive computer memory due to the extensive meshing involved. However, in this research area, some interesting designs have been reported using full-wave analyzers and commercial software packages in [7, 8].

The transverse equivalent network (TEN) model is a promising CAD-tool for estimating the far-field radiation properties such as the directivity and radiation patterns of cavity resonance antennas [7, 9–13]. Its accuracy have been compared with the full-wave analysis methods such as MoM in [13–15]. It has also shown excellent agreement with other complicated methods based on Green's function calculations in [9, 10] or leaky-wave analysis in [16]. Yet, it is not time-consuming in comparison with the full-wave analysis methods such as FDTD, FEM or MoM. A rigorous analytic method, similar to the method introduced in [10], has been addressed in [17] which confirms the versatility of this method in predicting the far-field properties of this class of antennas. Another interesting method of homogenization of periodic structures, employed in the substrate and superstrate of antennas, has been developed and addressed in [18].

In this paper, the concept of the cavity-resonance antennas with artificial ground plane and dielectric superstrate is introduced first. This problem is formulated using the TEN model. Then, an in-house developed MoM code is presented which treats periodic strip grating on a grounded dielectric slab. This code is employed to design an artificial ground plane acting as an AMC at a certain frequency for x-polarized incident waves and as an artificial electric conductor (AEC) at twice that frequency for y-polarized incident waves. Next, this artificial ground plane is used in a cavity-resonance antenna resulting in a dual-band orthogonal polarized high-gain antenna.

2. TEN MODEL OF THE CAVITY RESONANCE ANTENNA

A horizontal electric Hertzian dipole embedded in an air-gap layer, over a ground plane at a height h, and covered by a dielectric superstrate layer is shown in Fig. 1. It is assumed that the ground plane surface,

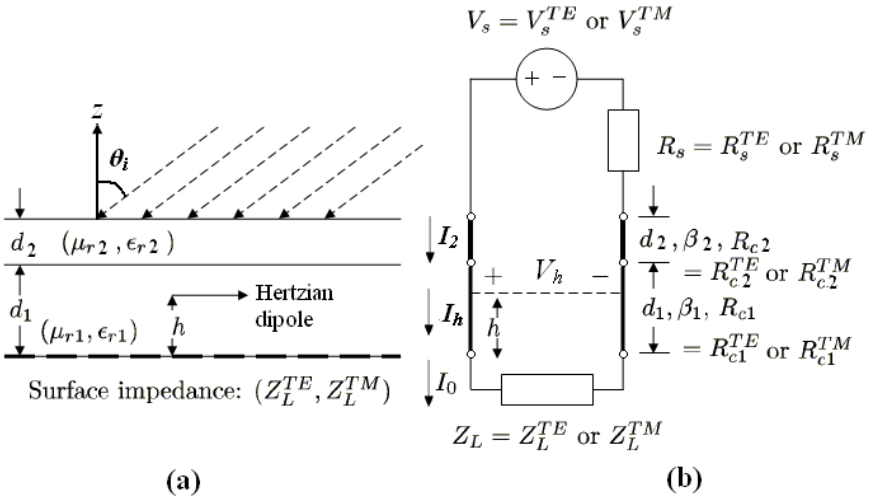

Figure 1. (a) Antenna configuration geometry and (b) TEN model of the antenna.

air gap layer and dielectric cover are infinite in the transverse direction. Using the TEN model, this antenna is simplified to the structure consisting of sections of transmission lines terminated by a load as shown in Fig. 1(b). In this model the electric Hertzian dipole is considered as a probe, which receives the electric field signal caused by the plane wave at far field. Having this approach, the applied electric field on this probe is proportional to the voltage V_h, which is the voltage at the distance h from the load impedance. V_h can be found using two sets of linear equations as follows [12].

$$\begin{bmatrix} V_s - I_2 R_s \\ I_2 \end{bmatrix} = \begin{bmatrix} A & B \\ C & D \end{bmatrix} \begin{bmatrix} I_0 Z_L \\ I_0 \end{bmatrix} \tag{1}$$

$$\begin{bmatrix} V_h \\ I_h \end{bmatrix} = \begin{bmatrix} A' & B' \\ C' & D' \end{bmatrix} \begin{bmatrix} I_0 Z_L \\ I_0 \end{bmatrix}, \tag{2}$$

where A, B, C and D are the elements of the ABCD matrix of the entire cascaded transmission lines and the load, while A', B', C' and D' are the elements of the ABCD matrix of the portion below the Hertzian dipole (Fig. 1). Other quantities shown in Fig. 1 are defined

as

$$\begin{aligned} V_s^{TE} &= 1, & V_s^{TM} &= V_s^{TE}\cos(\theta_i) \\ R_s^{TE} &= \eta_0/\cos(\theta_i), & R_s^{TM} &= \eta_0\cos(\theta_i) \\ R_{cn}^{TE} &= \eta_0\frac{\mu_{rn}}{\sqrt{\mu_{rn}\epsilon_{rn}-\sin^2(\theta_i)}}, & R_{cn}^{TM} &= \eta_0\frac{\sqrt{\mu_{rn}\epsilon_{rn}-\sin^2(\theta_i)}}{\epsilon_{rn}} \\ \beta_n &= k_0\sqrt{\mu_{rn}\epsilon_{rn}-\sin^2(\theta_i)}, & \eta_0 &= \sqrt{\mu_0/\epsilon_0}, \end{aligned} \tag{3}$$

where $n = 1$ and 2 are indices corresponding to the air gap and dielectric superstrate layer, respectively. Let's assume that the horizontal electric Hertzian dipole is placed at the origin and in the ρ_J direction as follows

$$\hat{\rho_J} = \hat{x}\cos(\phi_J) + \hat{y}\sin(\phi_J), \tag{4}$$

the corresponding far-field electric components are calculated as below

$$\begin{aligned} E^{TE} &= E_\phi = V_h^{TE}\hat{\rho_J}.\hat{\phi} = V_h^{TE}\sin(\phi_J-\phi) \\ E^{TM} &= E_\theta = V_h^{TM}\hat{\rho_J}.(\hat{\phi}\times\hat{z}) = V_h^{TM}\cos(\phi_J-\phi) \end{aligned} \tag{5}$$

which are consistent with the results obtained in [12]. Throughout this study, the antenna directivity is calculated using the following formula [9]

$$D(\theta,\phi) = \frac{4\left(\sin^2(\phi)|V_h^{TE}(\theta)|^2+\cos^2(\phi)|V_h^{TM}(\theta)|^2\right)}{\int_0^{\pi/2}\sin(\theta)\left[|V_h^{TE}(\theta)|^2+|V_h^{TM}(\theta)|^2\right]d\theta}. \tag{6}$$

3. MOM ANALYSIS OF THE PERIODIC CONDUCTING STRIPS ON A GROUNDED DIELECTRIC SLAB

Analysis of the scattering from periodic gratings has attracted the attention of many researchers [19–22]. Other types of periodic structures with two- or three-dimensional periodicity can be analyzed using different numerical techniques such as the ones introduced in [23–25]. They may also find interesting applications [26, 27].

In this section method of moment analysis of electromagnetic scattering by a periodic strip grating on a grounded dielectric slab, shown in Fig. 2, for arbitrary plane incident wave is presented. The extracted reflection properties using this method are employed to characterize impedance surface of this periodic structure for both TE^z and TM^z polarizations, and for various incident angles. The impedance surface is in turn used in TEN model of the cavity resonance antenna presented in the next section to extract its far-field radiation properties.

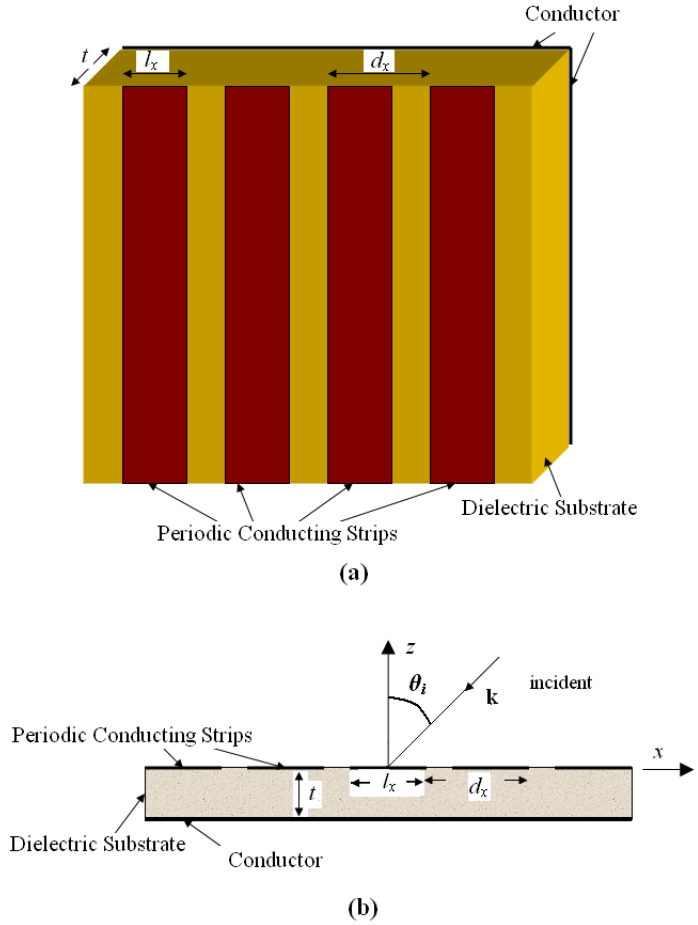

Figure 2. Periodic strip grating on a grounded dielectric slab. (a) 3-D view. (b) Side view.

3.1. Expansion of Electric Strip Currents into Entire-Domain Basis Functions

The x-directed electric surface current density over the 0th strip of the periodic conducting strips array is expressed as

$$J_x(x,y) = e^{-jk_{x0}x}e^{-jk_y y}\sum_{p=0}^{N_x} a_p f_{x_p}(x), \quad \text{for} \quad |x| \le \frac{l_x}{2} \tag{7}$$

$$J_y(x,y) = e^{-jk_{x0}x}e^{-jk_y y}\sum_{p=0}^{N_y} b_p f_{y_p}(x), \quad \text{for} \quad |x| \le \frac{l_x}{2} \tag{8}$$

where phase variations along x and y are defined with respect to the origin. Due to the periodicity in the x direction and according to Floquet's theorem corresponding phase constant in the x direction can be represented in a discrete form as

$$k_{x_m} = k_0 \sin(\theta_0)\cos(\phi_0) + \frac{2\pi m}{d_x} \tag{9}$$

where θ_0 and ϕ_0 determine the direction of the incident wave. The phase propagation along the y direction is

$$k_y = k_0 \sin(\theta_0)\sin(\phi_0). \tag{10}$$

The surface current can be expanded into a product of a series of cosine functions and a function satisfying edge condition [28]. The proper basis functions are selected as the ones introduced in [16, 17], i.e.,

$$f_{x_p}(x) = \sqrt{1-\left(\frac{2x}{l_x}\right)^2}(j)^p \cos\left(\frac{p\pi}{l_x}\left(x+\frac{l_x}{2}\right)\right), \tag{11}$$

$$f_{y_p}(x) = \left[\sqrt{1-\left(\frac{2x}{l_x}\right)^2}\right]^{-1}(j)^p \cos\left(\frac{p\pi}{l_x}\left(x+\frac{l_x}{2}\right)\right). \tag{12}$$

The Fourier transform of the pth x- or y-directed surface current basis function $f_{s_p}(x)$ is signified as $\widetilde{f_{s_p}}(k_x)$ and calculated as

$$\widetilde{f_{s_p}}(k_x) = \int_{-l_x/2}^{l_x/2} f_{s_p}(x) e^{jk_x x} dx, \tag{13}$$

where s can be x or y. Thus, the Fourier transform of Eqs. (11) and (12) are

$$\widetilde{f_{x_p}}(k_x) = \frac{\pi l_x}{2}\left[(-1)^p \frac{J_1(\frac{p\pi+k_x l_x}{2})}{p\pi+k_x l_x} + \frac{J_1(\frac{p\pi-k_x l_x}{2})}{p\pi-k_x l_x}\right] \tag{14}$$

$$\widetilde{f_{y_p}}(k_x) = \frac{\pi l_x}{4}\left[(-1)^p J_0(\frac{p\pi+k_x l_x}{2}) + J_0(\frac{p\pi-k_x l_x}{2})\right]. \tag{15}$$

The Fourier transforms of the surface currents presented above, are used in the next part, where spectral domain analysis is studied.

3.2. Spectral Electric Field Radiated by Strip Current

Upon Fourier transforming the electric surface current discussed above, into the spectral k_x domain, we have

$$\widetilde{\vec{J}}(k_{x_m}) = \hat{a_x} \sum_{p=0}^{N_x} a_p \widetilde{f_{x_p}}(k_{x_m}) + \hat{a_y} \sum_{p=0}^{N_y} b_p \widetilde{f_{y_p}}(k_{x_m}), \qquad (16)$$
$$m = \cdots, -1, 0, 1, \cdots.$$

This surface current corresponds to the discrete spectrum of the periodic structure. The $\widetilde{f_{s_p}}(k_{x_m})$ serves as the driving excitation for the grounded dielectric bare slab without the strips. The spectral field radiated by this spectral basis strip current (located in the layer above the slab) into the region above the grounded substrate is obtained from the numerical Green's function of the unloaded multilayer structure [18, 19], i.e.,

$$\widetilde{E_{w_p}^{J_s}}(k_{x_m}) = \widetilde{G_{E_w}^{J_s}} . \widetilde{f_{s_p}}(k_{x_m}). \qquad (17)$$

where the w subscript may denote either x or y component of the spectral E-field, and the superscript J_s signifies the type and component of the excitation current. The superscript of the Green's function $\widetilde{G}$ indicates the current source type and component, while the subscript represents the field type and component.

3.3. Spatial Electric Field Radiated by Entire Strip Array

Due to the periodicity along x with period d_x, the inverse transform from spectral k_x to spatial x domain only requires a summation over discrete spectral components defined in Eq. (10). Hence, the inverse transform of the spectral electric field of Eq. (17) is written as

$$\hat{u} E_{u_p}^{J_s} = \frac{1}{d_x} \sum_m \left[\hat{a}_x \widetilde{E_{x_p}^{J_s}}(k_{x_m}) + \hat{a}_y \widetilde{E_{y_p}^{J_s}}(k_{x_m}) \right] e^{-jk_{x_m}x}, \qquad (18)$$
$$m = \cdots, -1, 0, 1, \cdots.$$

where $\hat{u}$ denotes 'transverse' components. The summation performs through all integers of m. In fact, Eq. (18) constitutes the spatial transverse component of the electric field radiated by the s-directed spatial pth basis strip current $f_{s_p}(x)$. Eventually, the total transverse spatial electric field radiated by both electric current components J_x

and J_y is expressed as

$$\hat{u}E_u^{J_s} = \hat{a_x}\sum_{p=0}^{N_x} a_p E_{x_p}^{J_x} + \hat{a_y}\sum_{p=0}^{N_y} b_p E_{y_p}^{J_y}. \tag{19}$$

3.4. Spectral Excitation Current Source and its Radiated Electric Field

Depending on the polarization of the incident plane wave on the strip array, different types of spectral excitation current sources are entailed. Let this excitation current source be denoted generally by $\widetilde{K_{x,y}^{ex}}$, where K can be either J (electric) or M (magnetic), and the subscript can be either x or y labeling the component of the current. In the same manner as was shown in Eq. (17), the spectral electric field radiated by this excitation source is expressed as

$$\widetilde{E_w^{ex}} = \widetilde{G_{E_w}^{K_s}}.\widetilde{K_{s_p}^{ex}} \tag{20}$$

evaluated at ($k_x = k_{x0}$, $k_y = k_{y0}$), being the forcing wavenumber of the incident plane wave, constituting the fundamental Floquet mode as well. The spatial field is correspondingly

$$\hat{u}E_u^{ex} = \left(\hat{a_x}\widetilde{E_x^{ex}} + \hat{a_y}\widetilde{E_y^{ex}}\right) e^{-jk_{x_0}x}, \tag{21}$$

which is in the form of the excitation plane wave pertaining to a single (fundamental) Floquet mode. This source field is determinable with a known excitation current $\widetilde{K_{x,y}^{ex}}$.

The total spatial electric field in the region above the strip array is ultimately written as

$$E_u^{tot} = E_u^{J_s} + E_u^{ex} \tag{22}$$

3.5. Galerkin Weighting of Boundary Condition

The boundary condition requires the component of the total electric field tangential to the PEC strips to vanish on the strip surface (at $z = 0$). Applying this boundary condition on zeroth strip results in

$$E_u^{tot}\left(-\frac{l_x}{2} \le x \le \frac{l_x}{2}\right) = 0 \tag{23}$$

Upon performing Galerkin weighting, a total number of equations that equals the number of unknown coefficients of the basis functions

expanding the strip currents are generated. This system of equation can be cast into a matrix equation:

$$[\bar{Z}][\bar{I}\,] = [\bar{V}] \tag{24}$$

where the matrices involved in Eq. (24) are defined as follows. The elements of $[\bar{Z}]$ are determined as

$$Z_{qp} = \int_{-\frac{l_x}{2}}^{\frac{l_x}{2}} \hat{u} E_{u_p}^{J_s} \cdot \hat{s} f_{s_q}(x) dx, \tag{25}$$

where u is the transverse direction and consisting of both x and y directions. s is the direction of the current basis function and can be either x or y. The elements of $[\bar{I}\,]$ are unknown current basis function coefficients and are determined as

$$\left[\bar{I}\,\right] = \begin{bmatrix} a_0 \\ \vdots \\ a_{N_x} \\ b_0 \\ \vdots \\ b_{N_y} \end{bmatrix}_{N_x+N_y+2}, \tag{26}$$

The elements of $[\bar{V}]$ can be determined as

$$V_q = -\int_{-\frac{l_x}{2}}^{\frac{l_x}{2}} \hat{u} E_{u_p}^{ex} \cdot \hat{s} f_{s_q}(x) dx. \tag{27}$$

3.6. Numerical Results

In this part, some numerical results are shown to validate the in-house developed code based on method of moment (MoM) presented earlier in this section. Then, using this MoM code, the characteristics of a periodic strip grating on a grounded dielectric slab is studied versus frequency for various incident angles.

As the first example, a periodic structure is considered as shown in Fig. 2 with the dimensions of $l_x = 5\,\text{mm}$, $d_x = 10\,\text{mm}$ and $t = 1.59\,\text{mm}$. The dielectric is assumed to be lossless with relative permittivity of 2.5. Corresponding reflection phase versus frequency of this periodic structure due to normal incidence is shown in Fig. 3. As can be seen, there is an excellent convergence for different number of Floquet modes and basis functions. Similarly, there is good agreement ($< 8\%$) between the results obtained using the in-house MoM code and commercial

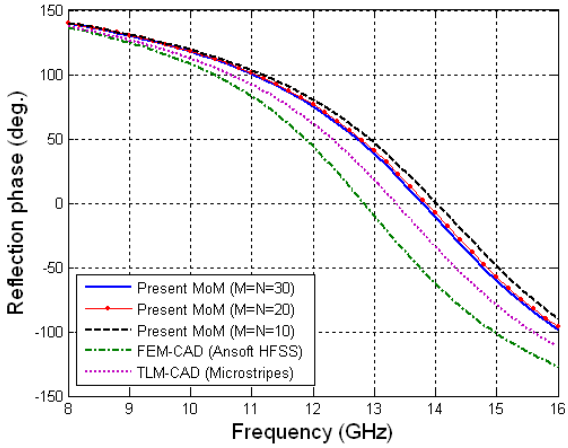

(a)

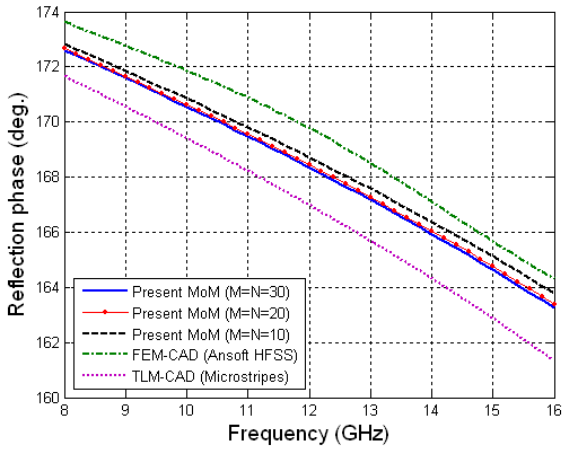

(b)

Figure 3. Reflection phase for normal incident angle, subject to the plane wave with (a) TE_y and (b) TM_y polarization. The corresponding structure is shown in Fig. 2 with dimensions of $l_x = 5\,\text{mm}$, $d_x = 10\,\text{mm}$ and $t = 1.59\,\text{mm}$. The dielectric is lossless with relative permittivity of 2.5. $2M + 1$ is the total number of Floquet modes. $2(N + 1)$ is the total number of basis functions in x and y direction, respectively ($N_x = N_y = N$).

FEM-CAD (Ansoft HFSS) and TLM-CAD (Microstripes). This type of frequency shift has been also observed for the reflection phases obtained for the designed AMC with metallic square patch unit cells in [31]. In [31], results obtained using commercial MoM-CAD software package (Ansoft Designer) were compared against those obtained using commercial FEM-CAD (Ansoft HFSS) and TLM-CAD (Microstripes) software packages. Interestingly, the reflection phase variation versus frequency shown in Fig. 3(a) is consistent with those shown in [31] in the sense that the resonant frequency (zero reflection phase) obtained using the FEM-CAD is the lowest while that obtained using the MoM-CAD is the highest.

Another periodic grating metallic structure is considered with the dimensions of $l_x = 5.54\,\text{mm}$, $d_x = 6\,\text{mm}$ and $t = 1.59\,\text{mm}$ (Fig. 2). The dielectric is assumed to be lossless with relative permittivity of 2.5. The reflection phase coefficients versus frequency for various incident angles and both TE_z and TM_z polarizations in principal planes ($\phi = 0^\circ$ and $\phi = 90^\circ$) are shown in Figs. 4 and 5. The reflection phases shown in Fig. 4 are responses to the incident wave having x-polarized electric field components (perpendicular to metallic strips). For this case, the resonant frequency (f_r), where the reflection phase is zero occurs at 9.5 GHz. The reflection phase shown in Fig. 5 are responses to the incident wave having y-polarized electric field components (parallel to metallic strips). For this case, however, the resonance does not occur and the reflection phase remains about PEC reflection phase (180°). The physical description of this fact will be explained in the next section.

4. ARTIFICIAL GROUND PLANE DESIGN

In this section, the antenna structure shown in Fig. 1 is considered with PEC, PMC or artificial ground planes. The far-field radiation properties of these different antenna configurations are studied using the TEN model described in Section 2.

4.1. Antenna with PEC Ground Plane

When the ground plane is PEC in Fig. 1(a), the load impedance in the transmission line model is zero ($Z_L = 0$). The antenna directivity versus air-gap height and superstrate thickness is shown in Fig. 6 for $\epsilon_r = 9.8$. The maximum directivities of this antenna configuration for different ϵ_r superstrate layers, are listed in Table 1. The same search space as illustrated in Fig. 6 is performed to obtain the maximum directivity for other values of superstrate dielectric

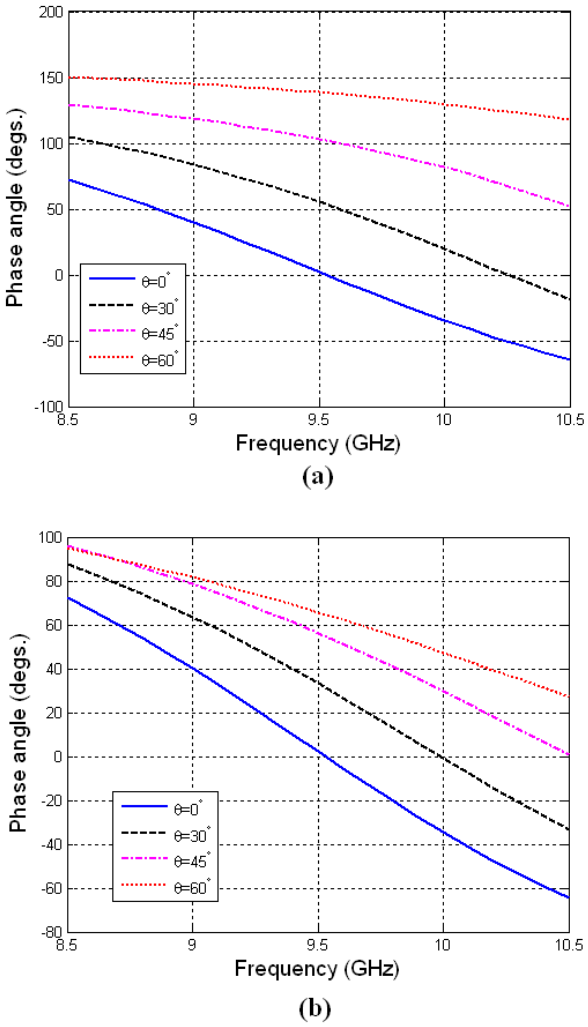

Figure 4. Reflection phase of the conducting periodic strip on grounded dielectric slab versus frequency for various incident angles. (a) TE^z at $\phi = 90°$ and (b) TM^z at $\phi = 0°$. Note that the electric field of the incident wave does not have any y-directed component. The corresponding structure is shown in Fig. 2 with the dimensions of $l_x = 5.54\,\text{mm}$, $d_x = 6\,\text{mm}$ and $t = 1.59\,\text{mm}$ (Fig. 2). The dielectric is lossless with relative permittivity of 2.5.

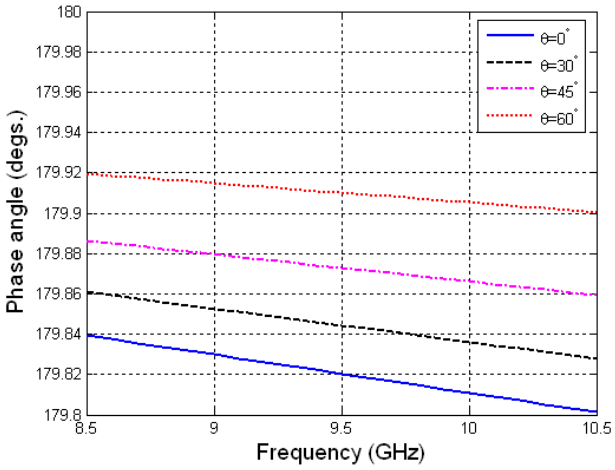

(a)

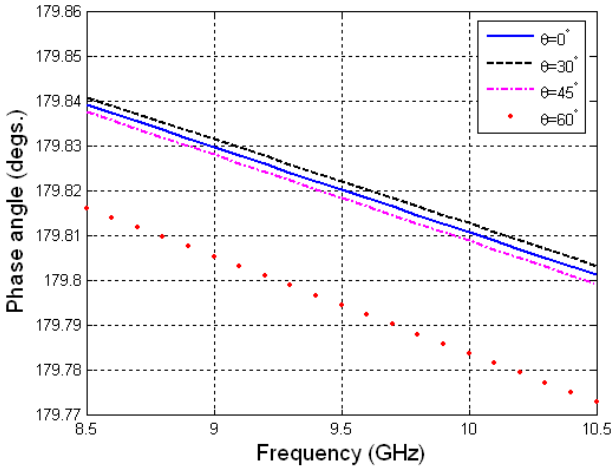

(b)

Figure 5. Reflection phase of the conducting periodic strip on grounded dielectric slab versus frequency for various incident angles. (a) TE^z at $\phi = 0°$ and (b) TM^z at $\phi = 90°$. Note that the electric field of the incident wave does not have any x-directed component. The corresponding structure is shown in Fig. 2 with the dimensions of $l_x = 5.54\,\text{mm}$, $d_x = 6\,\text{mm}$ and $t = 1.59\,\text{mm}$ (Fig. 2). The dielectric is lossless with relative permittivity of 2.5.

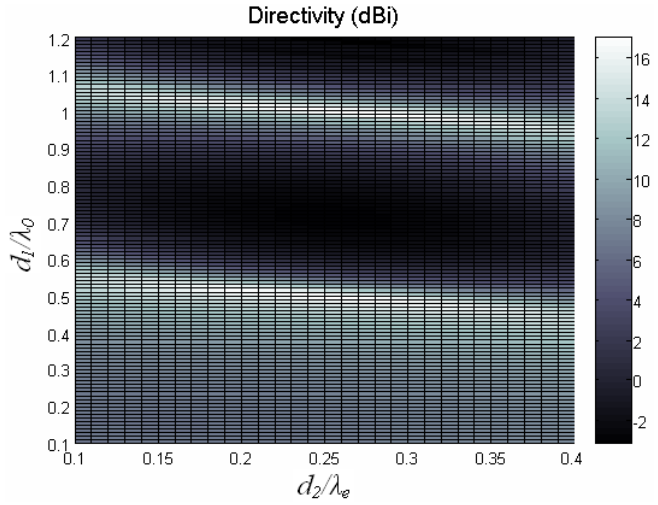

Figure 6. Directivity versus air-gap height (d_1/λ_0) and dielectric superstrate thickness (d_2/λ_e) for the cavity resonance antenna shown in Fig. 1 with PEC ground plane. Superstrate relative permittivity is $\epsilon_2 = 9.8$.

permittivity. These maxima are obtained for air-gap heights (d_1) and dielectric superstrate thicknesses (d_2) as shown in Tables 2 and 3. One should note that the values presented in Tables 2 and 3 correspond to the first resonance which introduces the lowest profile design. One also should note that $\lambda_e = \lambda_0/\sqrt{\epsilon_r}$, where λ_0 is free space wavelength at the operating frequency and ϵ_r is the relative permittivity of the superstrate, respectively. As can be seen in Tables 2 and 3, the maximum directivities are obtained for the dielectric thicknesses of about quarter-wavelength ($\sim \lambda_e/4$) and air-gap heights of about half-wavelength ($\sim \lambda_0/2$). This is consistent with the resonance conditions presented in [9]. For all cases studied in this part, the Hertzian dipole is placed at the height of $h/2$, as the maximum voltage V_h, supposedly, occurs at this height [9]. The corresponding radiation patterns of the above-mentioned antenna configurations are shown in Fig. 7.

The directivity of this antenna configuration ranges from 14.62 dBi to 16.88 dBi, for the superstrate having the lowest relative permittivity (5.5) to the highest relative permittivity (9.8). This is consistent with the previous studies such as [7, 8].

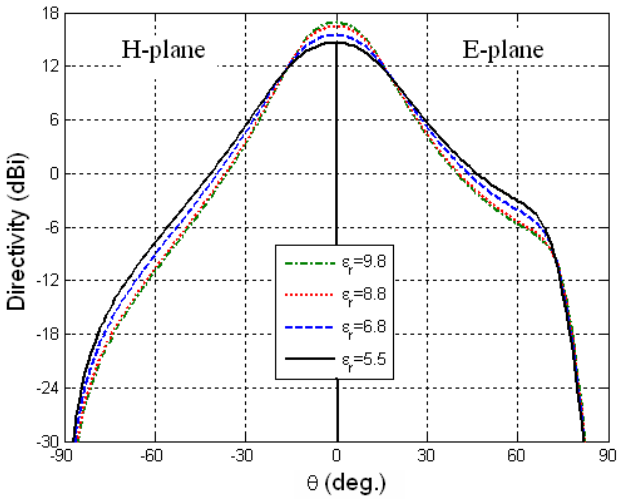

Figure 7. Radiation patterns of the antenna shown in Fig. 1 with PEC ground plane for different superstrate relative permittivities.

4.2. Antenna with PMC Ground Plane

When the ground plane is PMC in Fig. 1(a), the load impedance in the transmission line model is imaginary infinity ($Z_L = j\infty$). The antenna directivity versus air-gap height and superstrate thickness is shown in Fig. 8 for $\epsilon_r = 9.8$. The same search space as illustrated in Fig. 8 is performed to obtain the maximum directivity for other values of superstrate dielectric permittivity. The maximum directivities of this antenna configuration for various superstrate layers with different dielectric permittivities, are listed in Table 1. These maxima are obtained for air-gap heights (d_1) and dielectric superstrate thicknesses (d_2) as addressed in Tables 2 and 3. The values presented in Tables 2 and 3 correspond to the first resonance which introduces the lowest profile design. As can be seen in Tables 2 and 3, the maximum directivities are obtained for both air-gap heights and dielectric thicknesses of about quarter-wavelength of their corresponding media. For all cases studied in this section, the Hertzian dipole is placed on the PMC ground plane, as the maximum voltage V_h occurs at this height. The corresponding radiation patterns of the above-mentioned antenna configurations are shown in Fig. 9.

The directivity of this antenna configuration ranges from 12.11 dBi to 14.18 dBi, for the superstrate having the lowest relative permittivity (5.5) to the highest relative permittivity (9.8). The directivity in each case has been decreased at least by about 2.5 dB, compared to

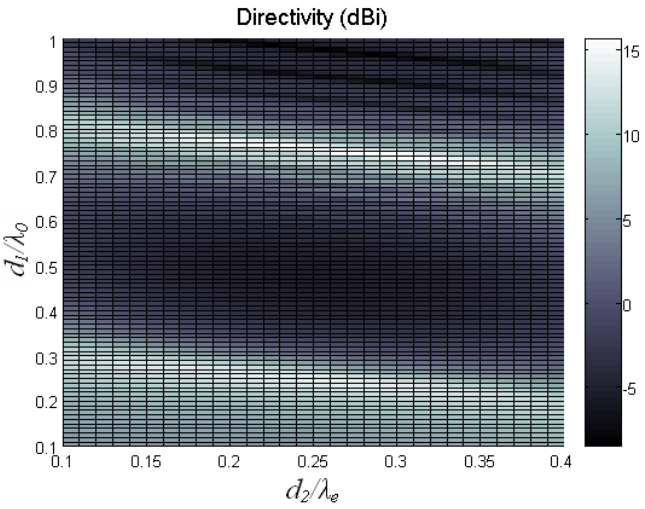

Figure 8. Directivity versus air-gap height (d_1/λ_0) and dielectric superstrate thickness (d_2/λ_e) for the cavity resonance antenna shown in Fig. 1 with PMC ground plane. Superstrate relative permittivity is $\epsilon_2 = 9.8$.

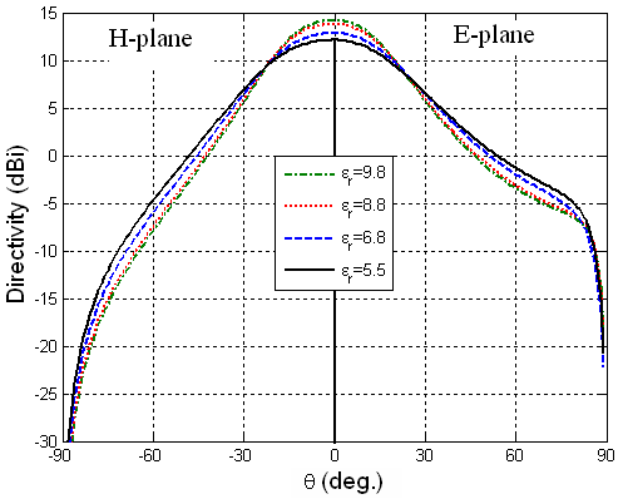

Figure 9. Radiation patterns of the antenna shown in Fig. 1 with PMC ground plane for different superstrate relative permittivities.

its counterpart with PEC ground plane. This is consistent with the previous studies using FEM-CAD full wave analysis (Ansoft-HFSS) for such class of antennas [4, 5].

4.3. Antenna with Artificial Ground Plane

The periodic strip grating on a grounded dielectric slab is considered as the artificial ground plane in this paper as shown in Fig. 2. The in-house developed MoM code presented in Section 3, was employed to design the artificial ground plane here. The dimensions of the periodic strip grating on the grounded dielectric slab are as follows. Periodicity (d_x) is 6 mm, strip width (l_x) is 5.54 mm, and the dielectric thickness (t) is 1.6 mm. The relative permittivity of the dielectric is 2.5. This artificial ground plane works in two different modes, namely AMC and AEC. This ground plane acts as an AMC for the x-polarized incident wave showing reflection phase of zero at normal incidence. As well it acts as an AEC for the y-polarized incident wave showing reflection phase close to 180°. These two modes are studied below in more details. The results presented in this section are obtained at frequencies of 9.5 and 19.0 GHz for AMC and AEC modes, respectively.

4.3.1. Antenna with Artificial Ground Plane in AMC Mode

The reflection phase versus incident angle is shown in Fig. 10 for both TE^z and TM^z polarizations, when the artificial ground plane works in AMC mode. In this mode, the electric field of the incident wave is x-directed. Intuitively, this is expected, since the periodic strips exhibits capacitive behavior to the x-polarized incident wave [32]. This capacitance is in parallel with the grounded dielectric slab having inductive characteristics. Therefore, the resonance occurs and the periodic structure demonstrates reflection phase close to zero, resulting in a high impedance surface. Surface impedances corresponding to both TE and TM polarizations are shown in Fig. 11. In fact these surface impedances are the load impedance in the TEN model (Fig. 1) and they have been calculated as follows [15],

$$Z_L^{\mathrm{TM}} = Z_0^{\mathrm{TM}} \frac{1 + \Gamma_{\mathrm{TM}}}{1 - \Gamma_{\mathrm{TM}}} \tag{28}$$

where Z_0^{TM} is the characteristic impedance of the air-gap region. The same formula applies for the TE polarization. One should note that the load impedance is both polarization and angular dependent.

As can be seen in Fig. 11, the AMC surface impedance is high at normal incidence. However, at corresponding grazing angles the

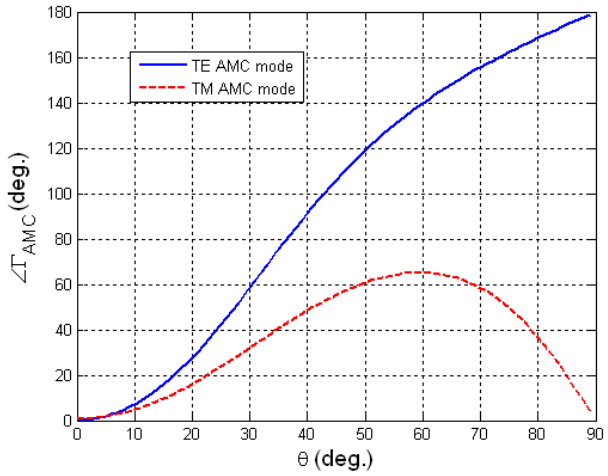

Figure 10. Reflection phase versus incident angles of the structure shown in Fig. 2 in AMC mode with dimensions of $d_x = 6\,\text{mm}$, $l_x = 5.54\,\text{mm}$, and $t = 1.6\,\text{mm}$. The relative permittivity of the dielectric is 2.5 and the operating frequency is 9.5 GHz.

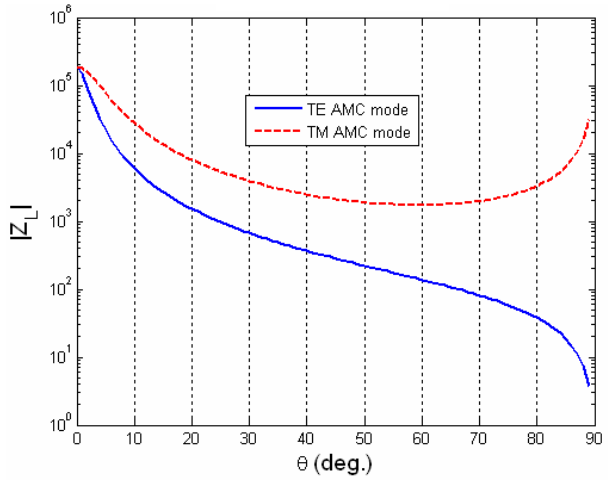

Figure 11. Surface impedance magnitude of the structure shown in Fig. 2 with dimensions of $d_x = 6\,\text{mm}$, $l_x = 5.54\,\text{mm}$, and $t = 1.6\,\text{mm}$. The relative permittivity of the dielectric is 2.5. Operating frequency is 9.5 GHz.

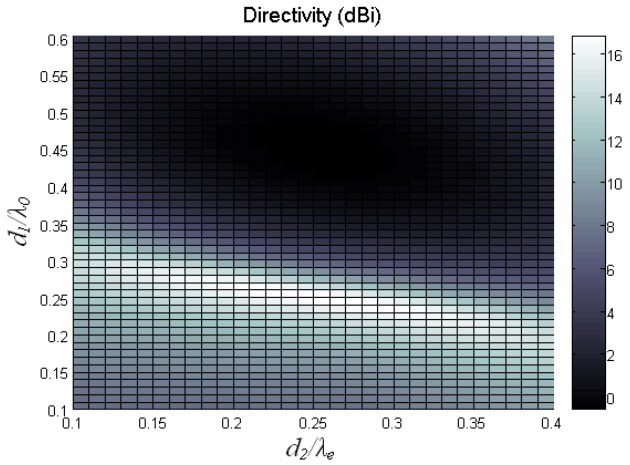

Figure 12. Directivity versus air-gap height (d_1/λ_0) and dielectric superstrate thickness (d_2/λ_e) for the cavity resonance antenna shown in Fig. 1 with AMC ground plane. Superstrate relative permittivity is $\epsilon_2 = 9.8$.

surface impedance is very low. This is consistent with the fact that reflection phase is about 180° for TE polarization (Fig. 10). Interestingly, the surface impedance magnitude is about 400 Ω for TM polarization as shown in Fig. 11. This is consistent with the fact that the reflection phase is almost uniform and about 90° at grazing angle for this polarization. Therefore, the surface impedance magnitude is about that of free space as supposed to be. The surface impedance phase is 90° and constant over the incident angles. Thus, the surface is high impedance and inductive. This is consistent with the fact that the reflection coefficient phase is always positive from very close to zero at normal incidence to about 180° at grazing angles.

Consider the above-mentioned artificial ground plane in AMC mode, as described above, for the antenna configuration shown in Fig. 1. The excitation is an x-polarized electrical Hertzian dipole. The antenna directivity versus air-gap height and superstrate thickness is shown in Fig. 12 for $\epsilon_r = 9.8$. The maximum directivities of this antenna configuration for various superstrate layers with different dielectric permittivities, are listed in Table 1. These maxima are obtained for air-gap heights (d_1) and dielectric superstrate thicknesses (d_2) as addressed in Tables 2 and 3. The values presented in Tables 2 and 3 correspond to the first resonance which introduces the lowest profile design. As can be seen in Tables 2 and 3,

the maximum directivities are obtained for both air-gap height and dielectric thickness of about quarter-wavelength of their corresponding media. For all cases studied in this section, the Hertzian dipole is placed on the AMC ground plane, as the maximum voltage V_h occurs at this height. The corresponding radiation patterns of the above-mentioned antenna configurations are shown in Fig. 13.

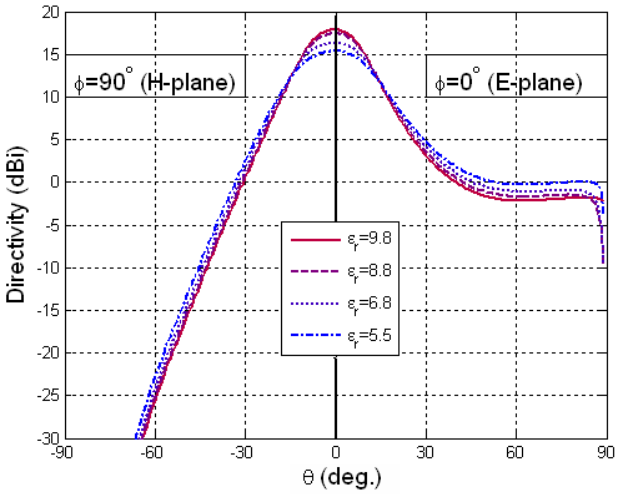

Figure 13. Radiation patterns of the antenna shown in Fig. 1 with AMC ground plane for different superstrate relative permittivities.

The directivity of this antenna configuration ranges from 15.38 dBi to 17.89 dBi, for the superstrate having the lowest relative permittivity (5.5) to the highest relative permittivity (9.8). This shows significant improvements, since in each antenna of this class with the introduced AMC ground plane, not only the air-gap height has been reduced by about half compared to its counterpart with a PEC ground plane, leading to low-profile design, but also the directivity has been increased by about 1 dB. This is not the case for antennas with PMC ground plane, and this property can be attributed to the angular polarization dependency of the AMC surface, acting similar to PMC at close-to-normal incident angles while similar to PEC at grazing incident angles.

4.3.2. Antenna with Artificial Ground Plane in AEC Mode

The reflection phase versus incident angle is shown in Fig. 14 for both TE^z and TM^z polarizations, when the artificial ground plane works in AEC mode. In this mode, the electric field of the incident wave is y-directed. The periodic strips exhibits inductive

behavior to the y-polarized incident wave [32]. This inductance is in parallel with the grounded dielectric slab having inductive characteristics, too. Therefore, the resonance does not occur. Instead, the equivalent inductance of the two parallel inductances introduces a lower inductance value resulting in a low impedance surface. Surface impedances corresponding to both TE and TM polarizations are shown in Fig. 15. As before, these surface impedances are the load impedance in the TEN model (Fig. 1) and they have been calculated using Eq. (28).

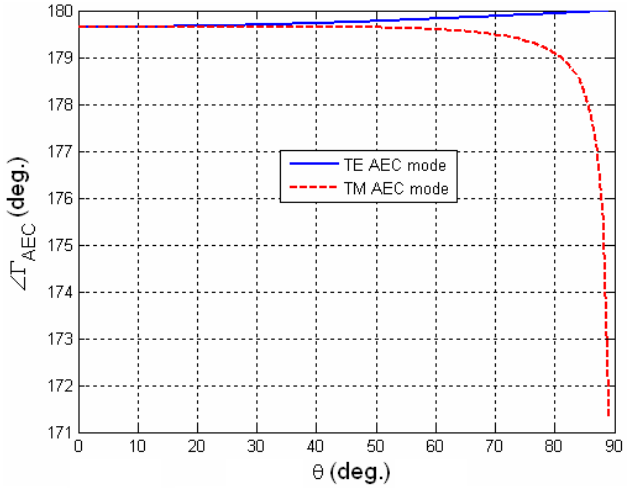

Figure 14. Corresponding reflection phase versus incident angles of the structure shown in Fig. 2 in AEC mode with dimensions of $d_x = 6\,\text{mm}$, $l_x = 5.54\,\text{mm}$, and $t = 1.6\,\text{mm}$. The relative permittivity of the dielectric is 2.5 and the operating frequency is 19.0 GHz.

As can be observed in Fig. 15, the corresponding surface impedances to AEC surface is low at normal incidence ($\sim 1\ \Omega$). For the TE polarization, the surface impedance magnitude decreases toward zero (PEC) at grazing angles, since the reflection phase increases toward 180°. For the TM polarization, however, the surface impedance magnitude increases at grazing angles, since the reflection phase decreases from 179.6° to 171°. Nevertheless, the impedance is still considered low ($\sim 30\ \Omega$). The surface impedance phase is 90° and constant over the incident angles. Thus, the surface is low impedance and inductive. This is consistent with the fact that reflection coefficient phase is always positive and about 180° for all incident angles.

Consider the above-mentioned artificial ground plane in AEC mode, as discussed above, for the antenna configuration shown in

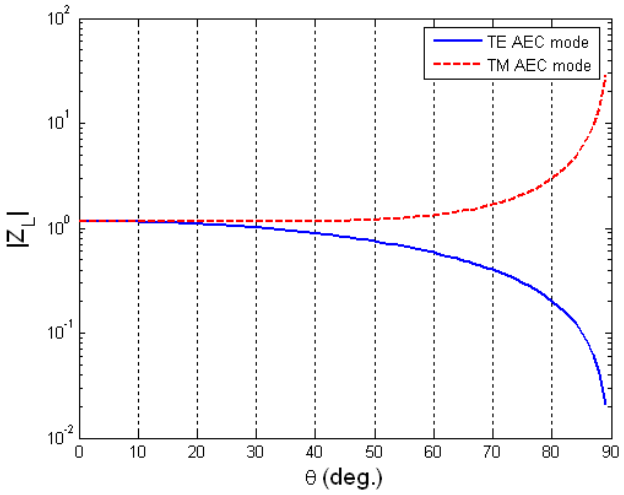

Figure 15. Surface impedance magnitude of the structure shown in Fig. 2 with dimensions of $d_x = 6\,\text{mm}$, $l_x = 5.54\,\text{mm}$, and $t = 1.6\,\text{mm}$. The relative permittivity of the dielectric is 2.5. Operating frequency is 19.0 GHz.

Fig. 1. The excitation is a y-polarized electrical Hertzian dipole. The antenna directivity versus air-gap height and superstrate thickness is shown in Fig. 16 for $\epsilon_r = 9.8$. The maximum directivities of this antenna configuration for various superstrate layers with different dielectric permittivities, are listed in Table 1. These maxima are obtained for air-gap heights (d_1) and dielectric superstrate thicknesses (d_2) as addressed in Tables 2 and 3. The values presented in Tables 2 and 3 correspond to the first resonance which introduces the lowest profile design. As can be seen in Tables 2 and 3, the maximum directivities are obtained for air-gap height about half-wavelength and dielectric thickness of about quarter-wavelength of their corresponding media. For all cases studied in this section, the Hertzian dipole is placed at the air-gap height of ($d_1/2$) from the AEC ground plane, as the maximum voltage V_h is supposed to occur at this height [9]. The corresponding radiation patterns of the above-mentioned antenna configurations are shown in Fig. 17.

The directivity of this antenna configuration ranges from 14.61 dBi to 16.87 dBi, for the superstrate having the lowest relative permittivity (5.5) to the highest relative permittivity (9.8). They are very close to their counterpart cases with a PEC ground plane. This is expected since the reflection coefficient phase of the AEC surface is very close to 180° (PEC surface) for a wide range of incident angles.

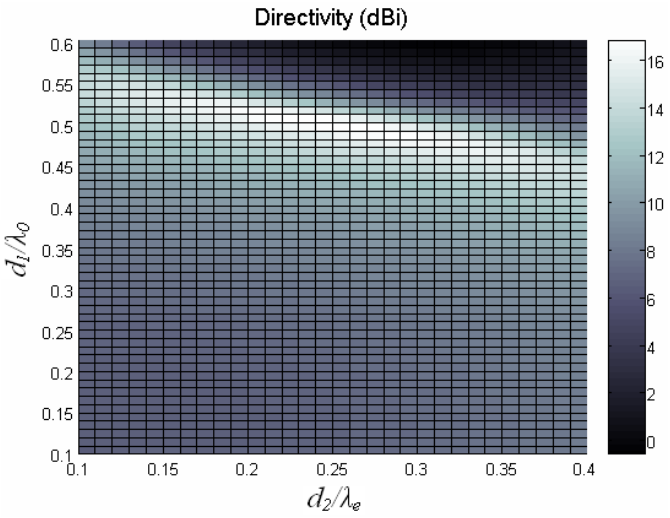

Figure 16. Directivity versus air-gap height (d_1/λ_0) and dielectric superstrate thickness (d_2/λ_e) for the cavity resonance antenna shown in Fig. 1 with AEC ground plane. Superstrate relative permittivity is $\epsilon_2 = 9.8$.

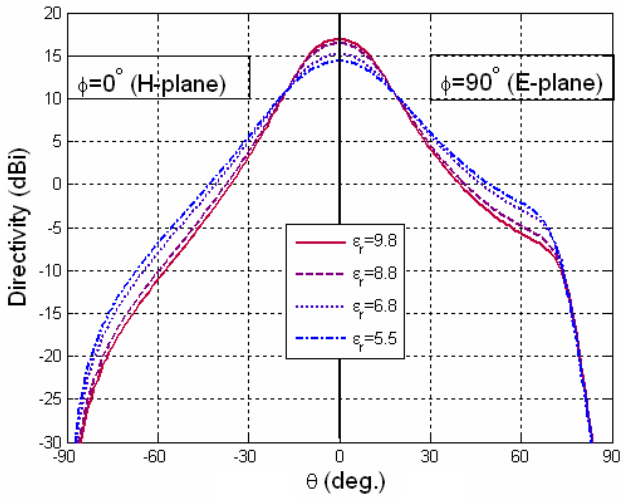

Figure 17. Radiation patterns of the antenna shown in Fig. 1 with AEC ground plane for different superstrate relative permittivities.

Table 1. Antenna directivities for different ground planes and dielectric superstrate permittivities.

ϵ_r	PEC	PMC	AMC	AEC
9.8	16.88	14.18	17.89	16.87
8.8	16.45	13.77	17.44	16.45
6.8	15.46	12.85	16.32	15.44
5.5	14.62	12.11	15.38	14.61

Table 2. Air-gap heights corresponding to maximum antennas directivities addressed in Table 1. The lengths are normalized to the free space wave length (d_1/λ_0).

ϵ_r	PEC	PMC	AMC	AEC
9.8	0.49	0.25	0.25	0.49
8.8	0.49	0.25	0.24	0.49
6.8	0.49	0.24	0.24	0.49
5.5	0.49	0.24	0.24	0.49

Table 3. Dielectric thicknesses corresponding to maximum antennas directivities addressed in Table 1. The lengths are normalized to the corresponding wave-length in each dielectric (d_2/λ_e).

ϵ_r	PEC	PMC	AMC	AEC
9.8	0.26	0.25	0.23	0.26
8.8	0.26	0.25	0.26	0.25
6.8	0.25	0.24	0.26	0.25
5.5	0.24	0.24	0.25	0.24

4.3.3. Antenna with Artificial Ground Plane in Dual-Mode

As it was discussed above, this antenna configuration can work in dual-frequency and dual-polarization mode. Top-view of such configuration is shown in Fig. 18. One should note that the air-gap height and superstrate dielectric thickness must be selected properly. It was shown that for the AMC and AEC mode the air-gap height is about a quarter and half wavelength, respectively. The thickness of the superstrate

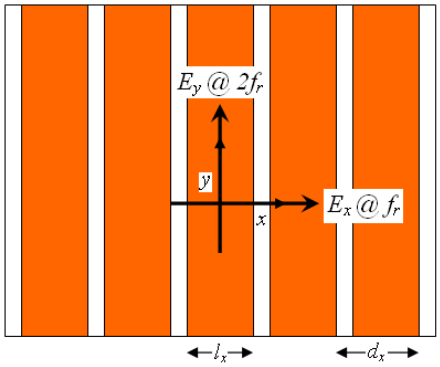

Figure 18. Top-view of the dual-polarized antenna configuration with artificial ground plane.

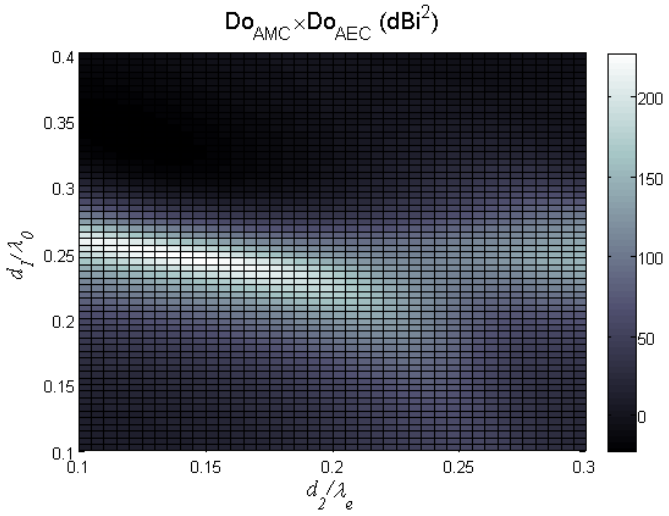

Figure 19. Product of the antenna directivities in AEC and AMC modes, versus air-gap height and dielectric thickness. Superstrate relative permittivity is $\epsilon_2 = 9.8$. The corresponding antenna configuration is shown in Fig. 18.

dielectric is about a quarter wavelength for both cases. Therefore, the AMC mode is selected for the lower frequency (9.5 GHz), and the AEC mode is selected for the upper frequency (19.0 GHz). One should note that the upper frequency is twice as the lower frequency. Therefore, the air-gap height can be kept the same for both frequencies. However, the

dielectric thickness cannot be maintained quarter-wavelength for both modes. Thus, an objective function consisting of the multiplication of the directivities in tow modes is considered. The function values versus dielectric thickness and air-gap height is shown in Fig. 19. One should note that the dielectric thickness and air-gap height are normalized to the corresponding wavelength media operating at the lower frequency (9.5 GHz). The maximum occurs at the corresponding values of $d_1 = 0.245\lambda_0$ and $d_2 = 0.135\lambda_e$ for lower frequency ($f_r = 9.5\,\text{GHz}$). The directivity of 14.05 dBi is achieved. At the higher frequency ($2f_r = 19.0\,\text{GHz}$), the directivity of 17.10 dBi is achieved. Obviously, the corresponding values of $d_1 = 0.49\lambda_0$ and $d_2 = 0.27\lambda_e$ are obtained. The results are summarized in Table 4. Dual-band orthogonally polarized configuration is obtained at the expense of about 3 dB loss in directivity for AMC mode. The above results were obtained when the electric Hertzian dipole is fixed at $h = \lambda/8$ above the ground. In this case, λ is the wavelength of the the lower frequency (9.5 GHz). This is because of the fact that in practical applications a single microstrip antenna can be used as the excitation for both modes. Therefore, both x-polarized and y-polarized electric Hertzian dipoles must have the same height from the artificial ground plane. The radiations patterns of this antenna configuration are shown in Fig. 20. These results are obtained when the relative permittivity of the superstrate dielectric is 9.8.

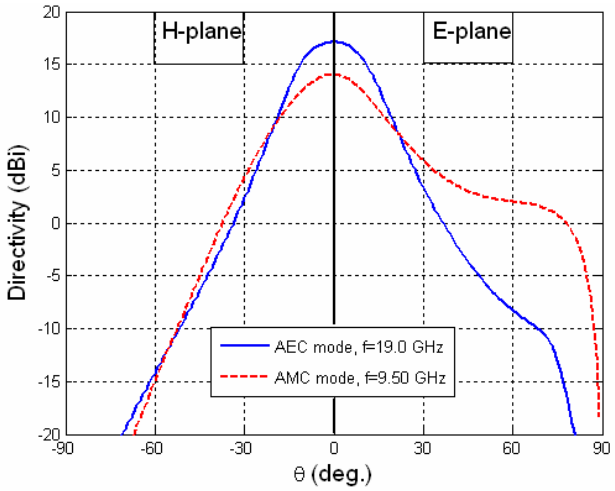

Figure 20. Radiation patterns of the designed antenna in two different modes. Superstrate relative permittivity is $\epsilon_2 = 9.8$.

Table 4. Properties of the optimized dual-band orthogonally polarized antenna.

Ground plane mode	Directivity	d_1/λ_0	d_2/λ_e	frequency
AMC	14.05 dBi	0.245	0.135	9.50 GHz
AEC	17.10 dBi	0.490	0.270	19.0 GHz

Interestingly, in spite of changing the electric Hertzian dipole positions, the antennas still demonstrate as high directivity as 17.1 dBi, slightly larger than the one shown in Table 4. Although the resonance condition introduced in [9] specifies certain height for the excitation probe, it has been shown for a certain range of probe heights the high directivity can be maintained [4, 33].

5. CONCLUSION

A conventional cavity resonance antenna, consisting of a Hertzian dipole embedded in an air-gap region, over a PEC or PMC ground plane and beneath the dielectric superstrate was analyzed using the TEN model. The advantage of selecting PMC over PEC ground place is in its more compact-size, where the antenna height is reduced by a factor of two. Its drawback is in a gain loss of 3 dB. An artificial surface was synthesized to be employed as the ground plane instead of the PEC or PMC ground plane. The artificial ground plane consisted of a grounded dielectric slab loaded by a periodic strip grating. This surface can act as an AMC at one frequency for a given polarization and as an AEC at the doubled frequency for the orthogonal polarization. In the introduced antenna configuration, when the ground plane works at AMC mode, not only the antenna height is reduced by half but also its directivity increased by about 1 dB compared to its conventional part with PEC ground plane. It also maintains the same features of the conventional antenna with the PEC ground plane, when it works at AEC mode. Using these features of the synthesized surface, a dual-band orthogonally polarized high-gain compact resonance cavity antenna was designed. One can maintain the thickness of the high-permittivity superstrate dielectric fixed to design a dual-band antenna at the expense of antenna directivity loss by about 3 dB at AMC mode at the lower frequency.

REFERENCES

1. "Special issue on artificial magnetic conductors, soft/hard surfaces, and other complex surfaces," *IEEE Trans. on Antennas and Propagat.*, Vol. 53, Jan. 2005.
2. Feresidis, A., G. Goussetis, S. Wang, and J. C. Vardaxoglou, "Artificial magnetic conductor surfaces and their application to low-profile high-gain planar antennas," *IEEE Trans. on Antennas and Propagat.*, Vol. 53, 209–215, Jan. 2005.
3. Wang, S., A. P. Feresidis, G. Goussetis, and J. C. Vardaxoglou, "High-gain subwavelength resonant cavity antennas based on metamaterial ground planes," *IEE Proc. - Microw. Antennas Propag.*, Vol. 153, No. 1, 1–6, Feb. 2006.
4. Foroozesh, A. and L. Shafai, "2-D truncated periodic leaky-wave antennas with reactive impedance surface ground planes," *Proc. IEEE Int. Symp.*, 15–18, Albuquerque, NM, July 9–14, 2006.
5. Foroozesh, A. and L. Shafai, "Size reduction in the high gain antennas with dielectric superstrate using artificial magnetic conductors," *Proc. ANTEM/URSI Int'l Symp.*, 523–526, Montreal, QC, July 17–19, 2006.
6. Foroozesh, A. and L. Shafai, "Size reduction of a microstrip antenna with dielectric superstrate using meta-materials: Artificial magnetic conductors versus magneto-dielectrics," *Proc. IEEE Int. Symp.*, 11–14, Albuquerque, NM, July 9–14, 2006.
7. Pirhadi, A., M. Hakkak, and F. Keshmiri, "Using electromagnetic bandgap superstrate to enhance the bandwidth of probe-fed microstrip antenna," *Progress In Electromagnetics Research*, PIER 61, 215–230, 2006.
8. Pirhadi, A., F. Keshmiri, M. Hakkak, and M. Tayarani, "Analysis and design of dual band high directivity EBG resonator antenna using square loop FSS as superstrate layer," *Progress In Electromagnetics Research*, PIER 70, 1–20, 2007.
9. Jackson, D. R. and N. G. Alexopoulos, "Gain enhancement methods for printed circuit antennas," *IEEE Trans. on Antennas and Propagat.*, Vol. 33, 976–987, Sep. 1985.
10. Alexopoulos, N. G. and D.R. Jackson, "Fundamental superstrate (cover) effects on printed circuit antennas," *IEEE Trans. on Antennas and Propagat.*, Vol. 32, 807–816, Aug. 1984.
11. Yang, H. Y. and N. G. Alexopoulos, "Gain enhancement methods for printed circuit antennas through multiple superstrates," *IEEE Trans. on Antennas and Propagat.*, Vol. 35, 860–863, July 1987.
12. Wu, X. H., A. A. Kishk, and A W. Glisson, "A transmission line

method to compute the far-field radiation of arbitrarily directed Hertzian dipoles in multilayer dielectric structure: Theory and applications," *IEEE Trans. on Antennas and Propagat.*, Vol. 54, 2731–2741, Oct. 2006.

13. Zhao, T., D. R. Jackson, J. T. Williams, H. Y. Yang, and A. A. Oliner, "2-D periodic leaky-wave antennas. Part I: Metal patch design," *IEEE Trans. on Antennas and Propagat.*, Vol. 53, 3505–3514, Nov. 2005.
14. Zhao, T., D. R. Jackson, and J. T. Williams, "2-D periodic leaky-wave antennas. Part II: Slot design," *IEEE Trans. on Antennas and Propagat.*, Vol. 53, 3515–3524, Nov. 2005.
15. Zhao, T., D. R. Jackson, J. T. Williams, and A. A. Oliner, "General formulas for 2-D leaky-wave antennas," *IEEE Trans. on Antennas and Propagat.*, Vol. 53, 3525–3533, Nov. 2005.
16. Jackson, D. R. and A. A. Oliner, "A leaky-wave analysis of the high-gain printed antenna configuration," *IEEE Trans. on Antennas and Propagat.*, Vol. 36, 905–910, July 1988.
17. Pirhadi, A. and M. Hakkak, "An analytical investigation of the radiation characteristics of infinitesimal dipole antenna embedded in partially reflective surfaces to obtain high directivity," *Progress In Electromagnetics Research*, PIER 65, 137–155, 2006.
18. Semichaevsky, A. and A. Akuyrtlu, "Homogenization of metamaterial-loaded substrates and superstrates for antennas," *Progress In Electromagnetics Research*, PIER 71, 129–147, 2007.
19. Uchida, K., T. Noda, and T. Matsunaga, "Spectral domain analysis of electromagnetic wave scattering by an infinite metallic grating," *IEEE Trans. on Antennas and Propagat.*, Vol. 35, 46–52, Oct. 1987.
20. Lee, C.-W. and H. Son, "Analysis of electromagnetic scattering by periodic strip grating on a grounded dielectric/magnetic slab for arbitrary plane wave incidence case," *IEEE Trans. on Antennas and Propagat.*, Vol. 47, 1386–1392, Sep. 1999.
21. Khalaj-Amirhosseini, M., "Scattering of inhomegenous two-dimensional periodic dielectric gratings," *Progress In Electromagnetics Research*, PIER 60, 165–177, 2006.
22. Watanabe, K. and K. Yasumoto, "Two-dimensional electromagnetic scattering of non-plane incident waves by periodic structures," *Progress In Electromagnetics Research*, PIER 74, 241–271, 2007.
23. Zheng, G., A. A. Kishk, A. W. Glisson, and A. B. Yakovlev, "A novel implementation of Maxwell's equations in the periodic finite-

difference time-domain method," *Progress In Electromagnetics Research*, PIER 59, 85–100, 2006.

24. Zheng, G., A. A. Kishk, A. W. Glisson, and A. B. Yakovlev, "Implementation of MUR's absorbing boundaries with periodic structures to speed up the design process using finite-difference time-domain method," *Progress In Electromagnetics Research*, PIER 58, 101–114, 2006.
25. Matsushima, A., Y. Momoka, M. Ohtsu, and Y. Okuno, "Efficient numerical approach to electromagnetic scattering from three-dimensional periodic array of dielectric spheres using sequantial accumulation," *Progress In Electromagnetics Research*, PIER 69, 305–322, 2007.
26. Dalili Oskouei, H., K. Forooraghi, and M. Hakkak, "Guided and leaky wave characteristics of periodic defected ground structures," *Progress In Electromagnetics Research*, PIER 73, 15–27, 2007.
27. Edalati, A., H. Boutayeb, and T. Denidni, "Band structure analysis of reconfigurable metallic crystals: Effect of active element," *J. of Electromagn. Waves and Appl.*, Vol. 21, No. 15, 2421–2430, 2007.
28. Butler, C. M.,"General solutions of the narrow strip (and slot) integral equations," *IEEE Trans. on Antennas and Propagat.*, Vol. 35, 1085–1090, Jan. 1985.
29. Sipus, Z., P.-S. Kildal, R. Leijon, and M. Johansson, "An algorithm for calculating Green's functions of planar, circular cylindrical and spherical multilayer substrates," *Applied Computational Electromagnetics Society (ACES) J.*, Vol. 13, No. 3, 243–254, Nov. 1998.
30. Ng Mou Kehn, M., M. Nannetti, A. Cucini, S. Maci, and P.-S. Kildal, "Analysis of dispersion in dipole-FSS loaded hard rectangular waveguide," *IEEE Trans. on Antennas and Propagat.*, Vol. 54, 2275–2282, Aug. 2006.
31. Foroozesh, A. and L. Shafai, "Investigation of reflection properties of reactive impedance substrates," *Proc. CCECE Int. Symp.*, 1881–1884, Saskatoon, SA, May 2005.
32. Munk, B., *Frequency Selective Surface: Theory and Design*, John Wiley & Sons, Inc., New York, 2000.
33. Foroozesh, A. and L. Shafai, "Effects of the excitation source position on the radiation characteristics of the antennas with a cover layer: A few case studies," *Proc. IEEE Int. Symp.*, 1507–1510, Albuquerque, NM, July 9–14, 2006.